

# Nano-Scale Simulation Technologies

● Toshiyuki Nakada   ● Kenichiro Aoki   ● Atsushi Furuya

*(Manuscript received June 30, 2005)*

Physical simulation technologies are employed in various areas of HDD development and design. These include structural analysis (vibration, impact shock), thermal fluid analysis (thermal deformation, heat dissipation), fluid analysis (head flight, airflow within a drive, contamination behavior), magnetic field analysis (read heads, write heads, motors), electromagnetic field analysis (signal transmission, EMI, immunity), and manufacturing process analysis (plating, ion milling, deposition). Thermal fluid analysis and manufacturing process analysis require nano-order precision to further increase HDD recording density. To meet this requirement, Fujitsu has developed and is actively using simulation techniques for analyzing head element protrusion and the ion milling and deposition processes. This paper focuses on the analysis of head element protrusion to minimize head flying height and the analysis of ion milling and deposition processes to further reduce the size of head element structures, with the overall aim of further increasing HDD recording density.

## 1. Introduction

Physical simulation technologies are used for many different aspects of HDD development and design. These include structural analysis (vibration, impact shock), thermal fluid analysis (thermal deformation, heat dissipation), fluid analysis (head flight, airflow within a drive, contamination behavior), magnetic field analysis (read heads, write heads, motors), electromagnetic field analysis (signal transmission, EMI, immunity), and manufacturing process analysis (plating, ion milling, deposition).

Given the increasingly higher HDD recording densities, we have reached a stage where HDD simulation technologies require nano-order precision. For instance, the annual reduction of head flying height has now reached the order of 10 nm, so an unevenness as small as 1 nm on the flying surface of the flying head slider would pose a problem. Moreover, for the read/write elements of magnetic heads to cope with extremely high-

density recording, their assemblies have been dramatically reduced in size, and nano-order dimensional precision is required since the maximum pattern width is only 100 nm. Fujitsu has developed new physical simulation technologies to solve the problems in coping with nano-order precision requirements.

Among the physical simulation technologies being applied to achieve increasingly higher recording densities in HDDs, this paper focuses on those employed to analyze head element protrusion and the processes of ion milling and deposition.

## 2. Analysis of head element protrusion

### 2.1 Purpose of analyzing head element protrusion

In recent years, head disk interface (HDI) technology has contributed significantly to reducing head flying height due to higher HDD

recording densities. Generally, the write and read elements and their protective shielding layer are made of metals that have a higher coefficient of thermal expansion than AlTiC, which is the base material of the heads. Therefore, rising temperature causes the head elements to protrude towards the disk, thus reducing the gap between the elements and disk surface. Now that the flying height is less than 10 nm, head elements protruding by just a few nm will increase the risk of contact between the head and disk.

The authors have divided this thermal protrusion into two types depending on whether it is caused by ambient temperature. The two types are Temperature-induced Pole-Tip Protrusion (T-PTP), which is caused by heat generated by the coils, and Write current-induced Pole-Tip Protrusion (W-PTP). T-PTP depends on differences in the coefficients of thermal expansion of head materials; W-PTP depends on temperature distribution due to the heat generated when current flows through the write coil.

In order to develop magnetic heads of high reliability, it is essential to maximize the precision of numerical analysis techniques by comparing measurement results for application to the elucidation of protrusion mechanisms and the prediction of deformation. However, research conducted on W-PTP and T-PTP until now has been limited to studying the considerable differences between W-PTP under actual operating conditions and W-PTP under natural convection conditions, based on either experimentation or simulation alone. Thus, the accuracy of simulation has yet to be properly verified through a comparison with experimentation, and protrusion mechanisms have yet to be adequately clarified.<sup>1)-5)</sup>

This paper first clarifies the differences in heat paths under two boundary conditions — the natural convection state with no disk and the flying state with a disk loaded — through numerical analysis and experimentation. Then, it discusses the verification of analysis accuracy for T-PTP and W-PTP, as well as for their mechanisms.

## 2.2 Numerical analysis model

**Figure 1** shows a model of the overall head prepared by the authors using an intricate mesh. This detailed model shows the structure of the magnetic head coil and the shield structures near the Giant Magneto Resistance (GMR) elements and other parts in detail. The model is intended for use in simulating heat generated from the coils. Actually measured values were used for thermal conductivity, thermal diffusivity, Young's modulus, and other physical parameters of the AlTiC, alumina, and permalloy used for the heads. We used ABAQUS, a commonly available, multipurpose finite element solver, for the analysis.

To calculate T-PTP, we assumed a uniform temperature distribution and analyzed thermal stress in the temperature range of 25°C (ambient temperature) to 70°C. For W-PTP calculations, we conducted coupled electric-thermal analyses to obtain temperature distributions while heat was being generated in the write coil and used the temperature distribution to analyze thermal stress. In order to compare temperature in the natural convection state with that in the flying state, we set up two boundary conditions. Under natural convection conditions, the coefficient of heat transfer on the slider surface in air is normally 20 to 30 W/m<sup>2</sup>K. Moreover, the thermal fluid analysis of a model including a suspension estimated the coefficient of heat transfer on the suspension side of the slider to be 270 W/m<sup>2</sup>K. We

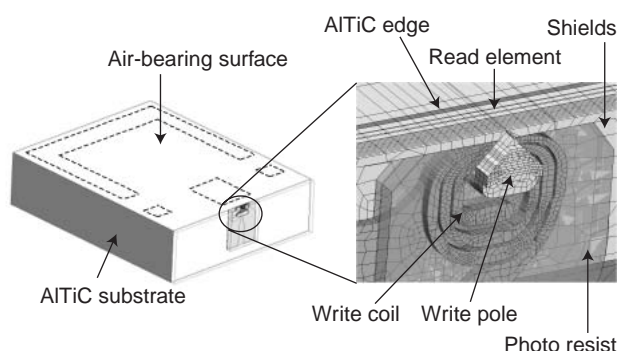


Figure 1  
FEM model for numerical analyses.

calculated the coefficient of heat transfer on the Air-bearing Surface (ABS) under flying conditions based on the method described in Reference 6), and then worked out the following formula for approximating the coefficient of thermal transfer on ABS, while ignoring minor terms.

$$h = \frac{K_{air}}{FH + 2 \cdot \beta \cdot \lambda \cdot P_0 / P} \quad (1)$$

In the equation above,  $h$  denotes the coefficient of heat transfer on ABS,  $k_{air}$  the conductivity of air,  $P$  the pressure on ABS,  $P_0$  the atmospheric pressure,  $FH$  the flying height, and  $\lambda$  the mean free path of air molecules.  $\beta$  denotes a constant with an assumed value of 1.5.

To calculate the coefficients of thermal transfer, we used the pressure distribution shown in **Figure 2 (a)** and computed the flying height on ABS by using the Reynold's equation solver. **Figure 2 (b)** shows the heat transfer distribution based on the coefficient of heat transfer calculated for ABS using Equation 1. As can be seen from Equation 1, a very small flying gap will cause tremendous heat transfer, as illustrated in Figure 2.

### 2.3 Results of numerical analysis and experiments

#### 1) Verification of W-PTP temperatures

We computed the temperature distribution for the previously mentioned boundary conditions.

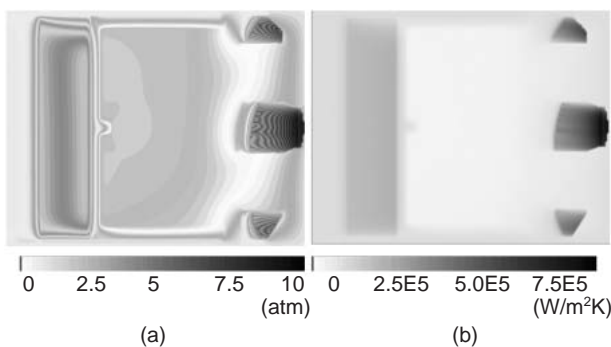


Figure 2  
(a) Pressure distribution on air-bearing surface. (b) Heat transfer distribution on air-bearing surface.

**Figure 3** shows the temperature distribution at the center of the magnetic head section for a write current of 60 mA DC. Figure 3 (a) shows the temperature distribution under natural convection conditions whereby the overall temperature of the elements has risen. Figure 3 (b) shows the temperature distribution under flying conditions with the greatest rise in temperature near the coils. We can see that the temperature distributions for both conditions are completely different.

To verify the accuracy of the numerical analysis, the authors compared the analysis results with actually measured values. Coil and MR element temperatures were calculated from measured changes in resistance. **Figure 4** compares the rises in temperature for different currents under natural convection conditions. **Figure 5** shows the same under flying conditions. From our results, we can see that the simulations under both boundary conditions satisfy the accuracy requirements.

We then applied the results of the calculations above to analyze the magnetic head heat paths. **Figure 6** shows the heat path under natural convection conditions; **Figure 7** shows the heat path under flying conditions. In both cases, a coil heat output of 100% is assumed. The results of this analysis indicate that most heat generated in the write coil escapes to the AlTiC substrate under both natural convection and flying conditions. Moreover, under natural

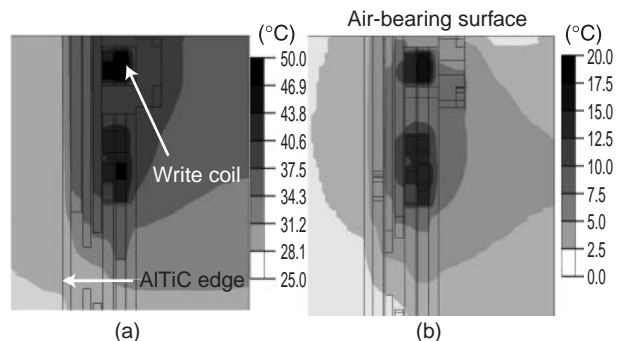


Figure 3  
Temperature distribution at DC write current of 60 mA.  
(a) Under natural convections.  
(b) Under flying conditions.

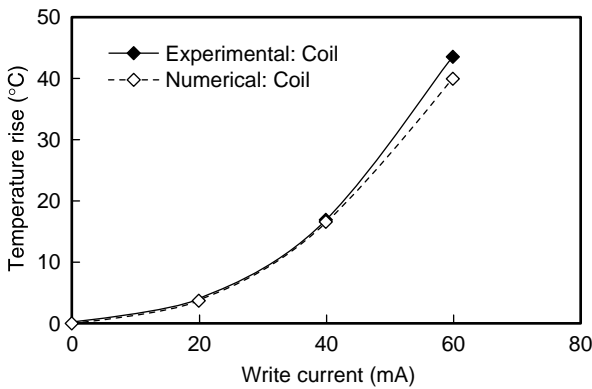


Figure 4 Comparison of temperature increase under natural convection conditions.

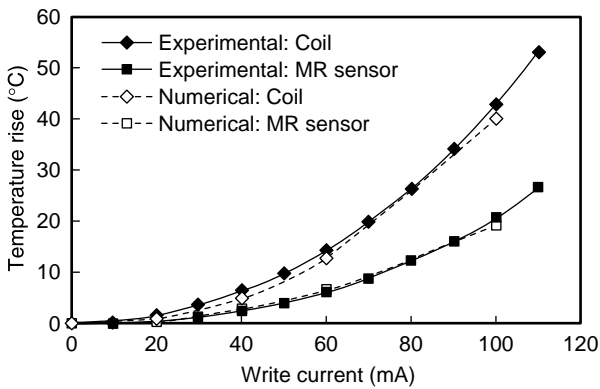
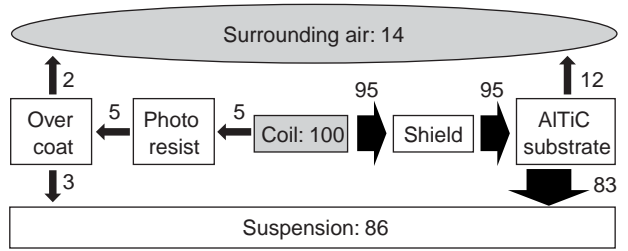


Figure 5 Comparison of temperature increase under flying conditions.

convection conditions, 86% of the heat passes to the suspension. Under flying conditions, heat passes to the rotating disk. The differences in heat paths occur because the heat paths have different coefficients of heat transfer. Since the situations under natural convection and flying conditions are completely different, the prediction of T-PTP during disk operation must be based on calculations made for the flying state.

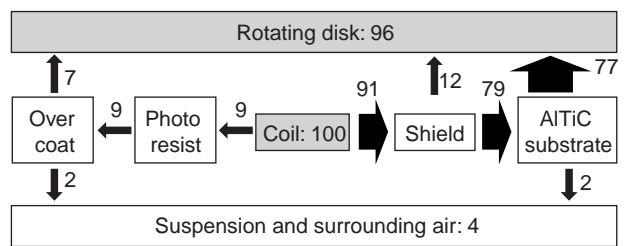
2) Verification of T-PTP and W-PTP

We analyzed T-PTP and W-PTP due to ambient temperature and the heat generated by coils, respectively, by means of finite element analysis. **Figure 8 (a)** shows the three-dimensional deformation near the write elements due to T-PTP when the ambient temperature rises to 45°C. From



Note) Arrow thickness represents the quantity of heat.

Figure 6 Heat path of head slider under natural convection conditions.



Note) Arrow thickness represents the quantity of heat.

Figure 7 Heat path of head slider under flying conditions.

these analysis results, we can consider thermal expansion in the coil, shield, and photoresist to be the principal causes of T-PTP. We then compared the analysis results with the results of optical interference measurements made along the ABS centerline (**Figure 9**). To compensate for the nonuniform optical characteristics in the measurements due to differences in the materials (e.g., alumina, AlTiC, permalloy), we coated the target area with Pd-Pt. In the comparison, a maximum protrusion of 3 nm was observed when the ambient temperature rose to 45°C. This suggests that using a detailed model and making highly reliable measurements of physical properties may provide accurate analysis results.

For W-PTP, we calculated the temperature distribution under flying conditions for use in computing W-PTP as shown in **Figure 8 (b)**. From the results, we can consider the temperature distribution due to heat generated by the coils to be the principal cause of W-PTP. We then compared

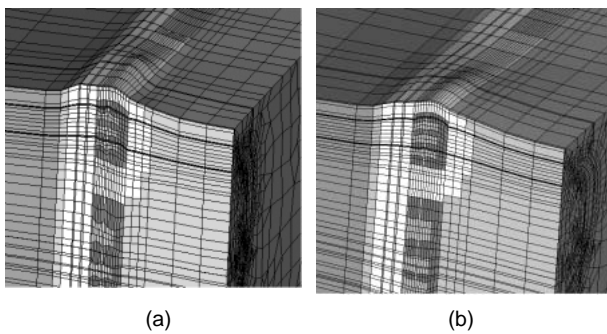


Figure 8  
Three-dimensional deformation in PTP.  
(a) T-PTP (Temperature-induced Pole-Tip Protrusion).  
(b) W-PTP (Write current-induced Pole-Tip Protrusion).

the results with the results obtained using Wallace spacing measurements (**Figure 10**). In this case, once the temperature distribution due to heat generated by the coils reached a steady state, the write current was switched off to stop it from generating heat. Thus, the coil temperature gradually dropped and the pace of W-PTP decreased over time. Figure 10 compares the numerical analysis results and measurements made during this process using the technique described above. In the comparison, we were able to obtain highly accurate analysis results for both steady and transient states by accurately estimating the ABS coefficient of heat transfer distribution under assumed flying conditions.

### 3. Analysis of ion milling and deposition processes

#### 3.1 Purpose of analyzing ion-milling and deposition processes

As HDD recording capacities have become higher, elements have become increasingly minute. GMR element heads read the data recorded on magnetic media by varying resistance in line with fluctuations in external magnetic fields. Given the continuous reduction in GMR element size, a GMR element width of about 100 nm is now required, thus necessitating very precise form control.

**Figure 11** shows the form of GMR elements and the related manufacturing process. The

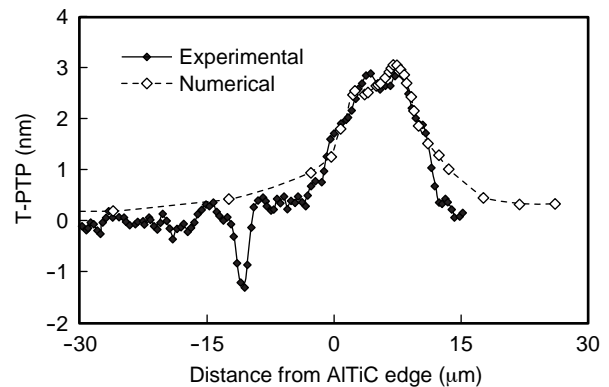


Figure 9  
Comparison of T-PTP along ABS centerline.

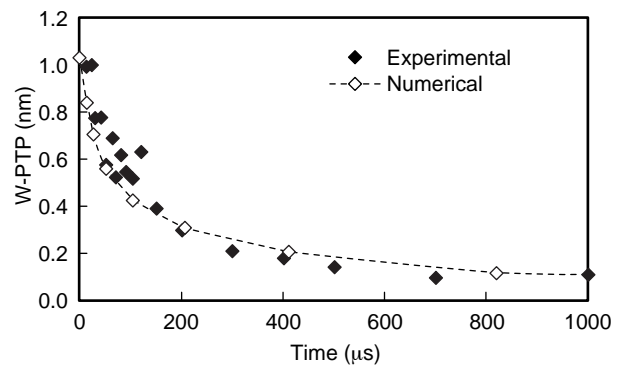


Figure 10  
Comparison of W-PTP in dynamic timescale.

elements are composed of the GMR layer (an electromagnetic conversion film), a hard bias film that applies a bias magnetic field to the GMR layer, and a shield that absorbs unwanted magnetic fields from media.

An insulator film and GMR film are formed on the shield [Figure 11 (a)], with a photoresist formed on the GMR film [Figure 11 (b)]. GMR film not protected by the photoresist is removed by ion milling [Figure 11 (c)], followed by the formation of a hard bias film and conducting lead film by vacuum deposition [Figure 11 (d)]. Next, the resist is removed for each part formed by deposition [Figure 11 (e)], followed by the formation of a resistance film and shield on the upper surface [Figure 11 (f)].

In the GMR element manufacturing process, since the ion milling that forms the GMR elements

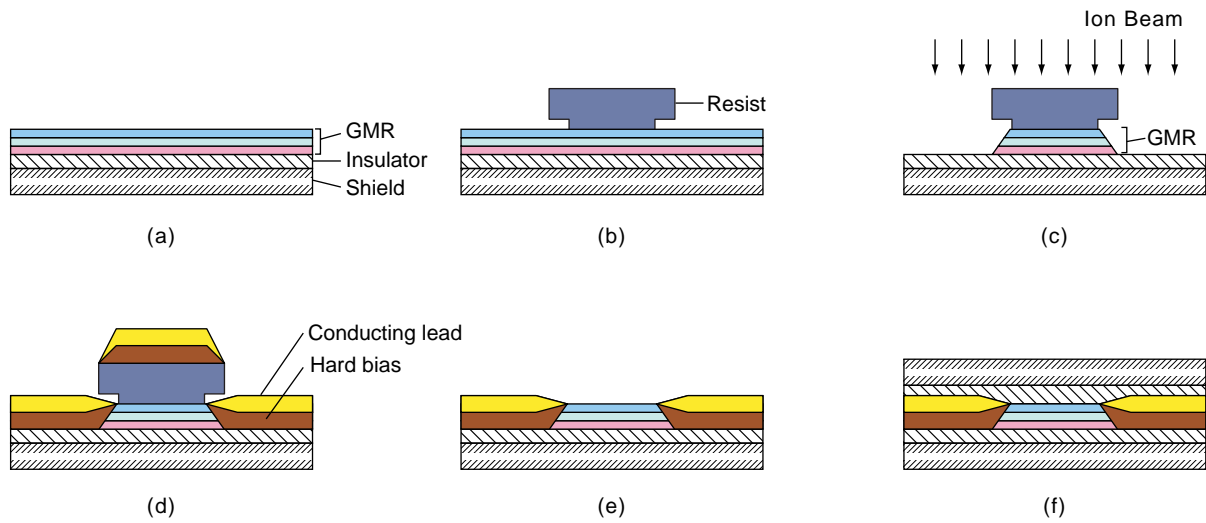


Figure 11  
 Illustration of HDD head process.  
 (a) Forming the GMR and insulator layer on the shield. (b) Forming the resist on the GMR layer. (c) Etching the GMR layer by ion milling. (d) Forming hard bias and lead layer. (e) Removing resist. (f) Forming the alternative insulator and shield layer.

[Figure 11 (c)] and deposition that forms the hard bias and conducting lead layers are particularly important in determining the GMR element form, accurately predicting the three-dimensional element forms resulting from ion milling and deposition based on a three-dimensional form simulation is essential for more efficient element development.

In the next subsection, we describe a model for three-dimensional topography simulation based on the Level Set method<sup>7)</sup> that is used to analyze the ion milling and deposition processes. Rather than conduct analysis based on Molecular Dynamics simulation, we constructed a model based on experimental measurements that allowed us to compute the three-dimensional process simulation within a realistic time.

### 3.2 Simulation of three-dimensional forms

The string model is used to handle topography changes through the iterative reconstruction of a triangular mesh. While the string model is advantageous in being able to handle sharp forms with a minimal amount of data, the reconstructed mesh that corresponds to the moving surface

is numerically unstable when the surface disappears due to the etching process. Therefore, in the present simulation, we used the Level Set method to handle three-dimensional topography changes with efficient numerical stability. The Level Set method expresses topography changes by assigning a level function  $\psi$  to lattice points that denote the distance from a surface, without considering the data structure of direct surfaces (**Figure 12**). Level function  $\psi$  is defined as 0 for a corresponding surface, negative for distance within a material, and positive for distances external to the material. This constant changes over time according to the Hamilton-Jacobi equation shown below.

$$\delta\psi/\delta t + F_{srf}|\nabla\psi| = 0 \tag{2}$$

Here,  $\nabla$  is the nabla operator. In the representation of surface forms, the Level Set method does not calculate the coordinate and node on the surface directly. For this reason, with the string model, the forming and erasure of triangular elements is unnecessary, thus making it possible to smoothly and accurately conduct processes for

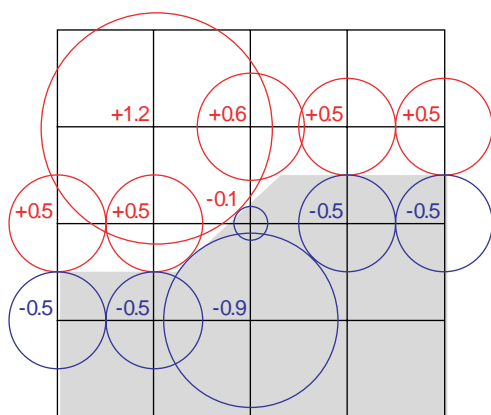


Figure 12  
Topology formulation of Level Set Method.

large changes in surface form (such as when forming holes).

In Equation (2),  $F_{srf}$  denotes the perpendicular velocity of the surface and is determined by the physical mechanism of surfaces in each manufacturing process. The following describes a physical model of surface motion speed and the related calculations.

### 3.3 Physical model of ion-milling and deposition processes

Ion milling is a micro-process for the physical etching of materials by using an ion beam. Ar gas is converted to plasma, accelerated by electrodes, and then used to irradiate the surface to be etched. Deposition is a process of forming a film on a substrate. Inert gas is introduced into a vacuum while voltage is applied between the substrate (on which material is to be deposited) and the target (material to be deposited), then the substance resulting from collisions between the ionized gas and target is deposited on the substrate. In order to simulate these processes, it is necessary to compute the following:

- 1) Amounts of etching and deposition due to irradiation by ions and atoms
- 2) Amounts of ion irradiation and flux density of deposition particles at each target location  
Note that 1) above is dependent on the

microstructure of etched materials and the types of ions and atoms used for irradiation. While it is possible to calculate the differences due to materials by using calculation methods that are applied to molecular and other atomic level dynamics without experimentation, it is not possible to make predictions of solid forms greater than a few 10 s of nm, given the limited scale of these calculation methods. Consequently, we measured  $Er(\theta)$ , the etching rate in the equation below, for various materials and used the results to make a model for computing three-dimensional changes in form. We also inferred the possibility  $\beta_I$  that deposition particles and particles removed from the etching surface would be deposited on the first surface that is struck after following a linear path of flight. With such a model, the following equation can be used to express the speed of surface motion.

$$F_{srf}(x,y,z) = -\int I_{ion}(\theta,\varphi) Er(\theta)pd\theta d\varphi + \beta_I \int I_{redep}(\theta,\varphi) \cos(\theta)/pd\theta d\varphi \tag{3}$$

Here,  $(\theta, \varphi)$  denote the angles of elevation and orientation as viewed from each surface;  $I_{ion}(\theta, \varphi)$  and  $I_{redep}(\theta, \varphi)$  the flux densities of the ion beam and deposition particles, respectively; and  $Er(\theta)$  the etching rate of the surface material.

We will next examine the calculation of  $I_{ion}(\theta, \varphi)$  and  $I_{redep}(\theta, \varphi)$  for 2) above.

For irradiating elements having uneven parts with an ion beam, as shown in **Figure 13**, the irradiation status varies depending on the solid form, which varies with the surface position. Moreover, since the flux density of the ion beam on each surface depends on solid angles  $(\theta, \varphi)$ , a three-dimensional evaluation must be made to determine whether and what kind of a positional relationship exists between the surface and the ion source. This evaluation requires calculations concerning visibility that consume the greatest amount of time.

In this regard, we have developed a technique by applying the Z buffer method used in CAD to evaluate the visibility of three-dimensional

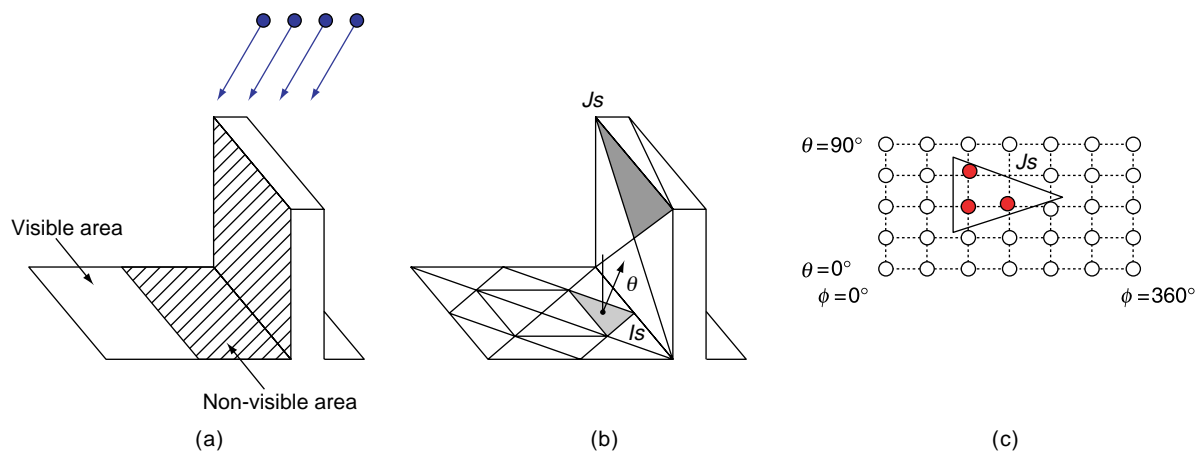


Figure 13  
 Illustration of visibility.  
 (a) Calculation methods using Z-buffer method. (b) Represent surface topography as a triangular mesh.  
 (c) Evaluation points covered by other surface components are updated.

structures. This technique is based on the following procedure.

- 1) Represent surface forms as a triangular mesh [Figure 13 (b)].
- 2) Divide solid angles of  $I_s$  surfaces into finite elements.
- 3) Place  $J_s$  surfaces into solid angles of  $I_s$  surface [Figure 13 (c)].
- 4) For solid-angle lattice points within surfaces, record distances between  $I_s$  and  $J_s$  surface.
- 5) Loop procedures 3 and 4 for  $I_s$  and  $J_s$ .

This procedure allows us to calculate the  $J_s$  surface direction from the  $I_s$  surface. Previously, in calculations and recording of the visibility of all surfaces from an  $I_s$  surface, visibility calculations were proportional to the 3<sup>rd</sup> power of the number of surface elements. However, these calculations may be speeded up by basing both calculation and recording on solid angles and making calculations proportional to the 2<sup>nd</sup> power of the number of surface elements.

The amounts of milling and deposition for the surface factors may be calculated as follows. First, since the ion beam orientation is determined by manufacturing conditions, calculations are only made for the ion-beam etching of surfaces that have no surfaces in the ion beam direction. More-

over, for etching surfaces that have a facing surface, the flux density for various factors is integrated for solid angles since there is supplementary deposition due to sputtering. With these considerations in mind, a visual evaluation procedure based on the Z buffer method may be used to handle changes in element form in relation to changes in three-dimensional solid forms.

### 3.4 Analysis of ion milling of GMR layer with overhanging resist

When the ion milling and deposition processes form a thin-film pattern, etched particles may be deposited on the resist wall. A resist with an overhang could be used to ensure that none of these particles remain after the resist is removed, but in such a case the effects of re-deposition and shadow from the resist may make it difficult to predict the etched shape. **Figure 14** shows the ion milling of a thin film on which a resist with an overhang has been formed, and for this situation, we verified the accuracy of the simulation through a comparison with measurement results. A single-layer GMR film was used as the thin film for read elements, although GMR film typically consists of several layers.

**Figure 15** shows a cross section of the GMR layer and re-deposition areas following ion

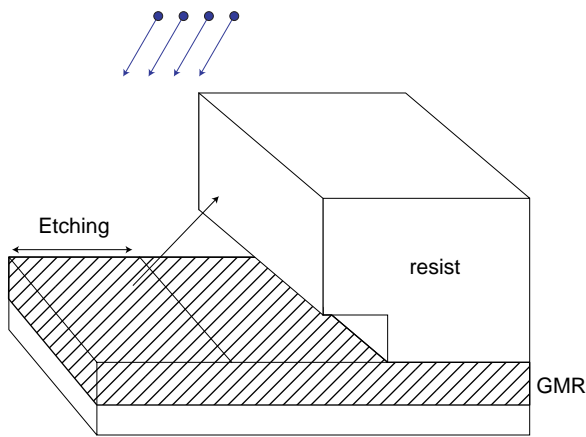


Figure 14  
Configurations of resist and GMR layer before ion milling process.

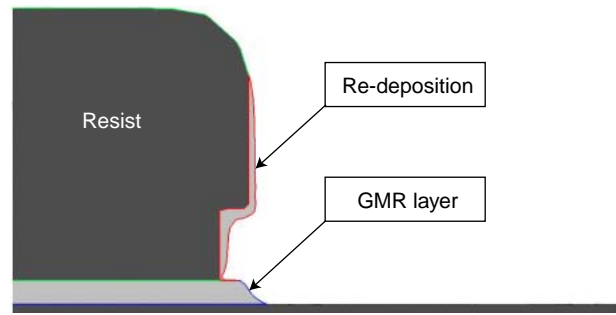


Figure 15  
Results of ion milling process simulation. Edge of GMR layer has a finite gradient due to shadowing effect of resist and effect of re-deposition of etched material.

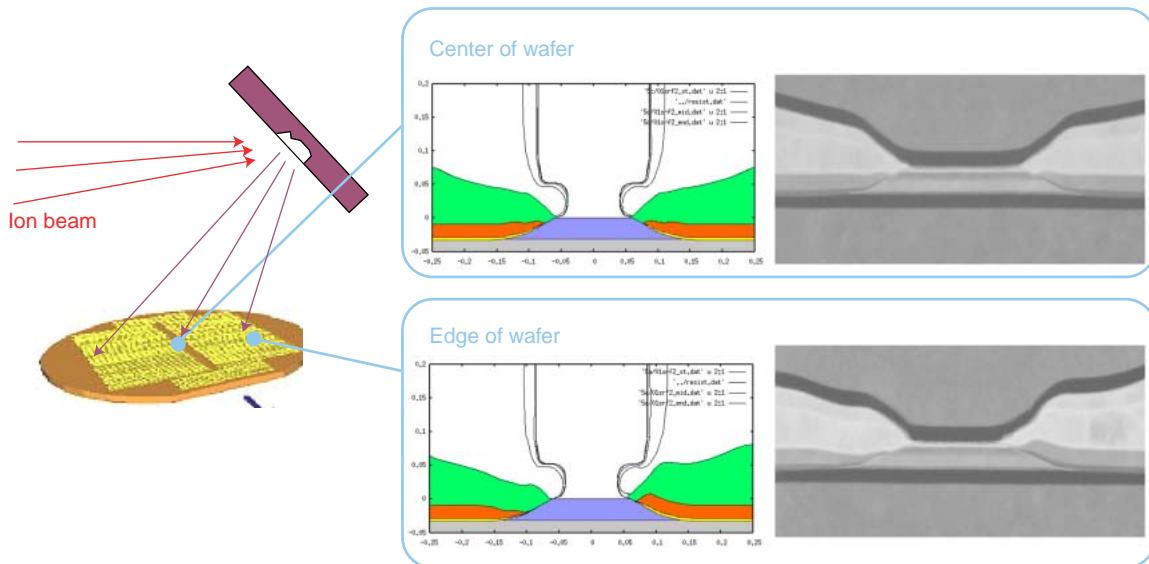


Figure 16  
Results of deposition simulation showing differences in form between center and edge of wafer.

milling for the simulation described above. Upon comparing the analysis and actual measurement results for the gradient of the edge of the GMR layer and the thickness of deposition on the resist wall, we found that the analysis and measurement results both showed a 20% discrepancy in the gradient of the GMR layer edge. Thus, when using a resist with an overhang, the edge of the GMR layer after etching is not vertical but has a gradient. Three-dimensionally speaking, this gradient forms due to the oblique shadowing effect of the

resist on the ion beam and the effect of re-deposition. Through three-dimensional calculations, we were able to accurately reproduce this situation.

We will now calculate the positional dependence of the sensor shapes in the Ion Beam Deposition (IBD) process by using the present simulation. IBD is a process whereby an ion beam irradiates the target material in a vacuum chamber and the free particles produced by the ion beam are adsorbed on a wafer to form a film. The shadow produced by concentrations of particles has a

significant effect on the final shape of elements after the process is completed. Also, since wafers are rotated while being formed in the IBD process, the shadow-affected parts keep changing through a process we were able to simulate. **Figure 16** shows the related results. The simulation very effectively reproduced a situation where the sensor shapes at the center of the wafer are both symmetrical and linear, while sensors at the wafer edge are asymmetrical and have bumps. The authors have used this simulation to improve the uniformity of sensor shape and performance of highly sensitive and stable sensors.

#### 4. Conclusion

This paper discussed the analysis of head element protrusion and the ion milling and deposition processes in detail. We confirmed that the results of both analyses were in good agreement with experimental results. We also proved that such analysis can be an effective tool in product design and process design directed at achieving even higher recording densities for

HDDs. In the future, we will continue to develop new simulation techniques and improve existing ones in order to contribute to even higher levels of HDD performance.

#### References

- 1) L. Pust, J. T. Ream, and S. Gangopadhyay: Thermomechanical head performance. *IEEE Trans. Magn.*, **38**, 1, p.101-106 (2002).
- 2) V. Nikitin, et al.: Spatial and temporal profiling of protrusion in magnetic recording heads. *IEEE Trans. Magn.*, **40**, 1, p.326-331 (2004).
- 3) B. K. Gupta, K. Young, S. K. Chilamakuri, and A. K. Menon: On the thermal behavior of giant magnetoresistance heads. *Trans. ASME, J. Tribology*, **123**, p.380-387 (2001).
- 4) T. Imamura, M. Yamagishi, and S. Nishida: In situ measurements of temperature distribution of air-bearing surface using thermography. *IEEE Trans. Magn.*, **38**, 5, p.2147-2149 (2002).
- 5) J. Xu, M. Kurita, and M. Tokuyama: Thermal analysis of a magnetic head. *IEEE Trans. Magn.*, **40**, 4, p.3142-3147 (2004).
- 6) L. Chen, D. B. Bogy, and B. Strom: Thermal dependence of MR signal on slider flying state. *IEEE Trans. Magn.*, **36**, 5, p.2486-2489 (2000).
- 7) D. Adalsteinsson and J. A. Sethian: A unified level set approach to etching, deposition and lithography. *J. Comp. Phys.*, **122**, 2, p.348-366 (1995).



**Toshiyuki Nakada** received the B.S. degree in Mechanical Engineering from Hiroshima Industrial Technology, Hiroshima, Japan in 1981. He joined Fujitsu Ltd., Kawasaki, Japan in 1981, where he has been working on process engineering. He is a manager of computational mechanical simulation projects at HDD technology development department in the Fujitsu storage products group.

E-mail: nakada.toshiyuk@jp.fujitsu.com



**Atsushi Furuya** received the Ph.D. in Physics from Kyushu University, Fukuoka, Japan in 2003. He joined Fujitsu Ltd., Kawasaki, Japan in 2003, where he has been engaged in research and development of a 3-dimensional process simulator for manufacturing MR head sensors of HDD devices. He is a member of the Magnetic Society of Japan (MSJ).

E-mail: furuya.atsushi@jp.fujitsu.com



**Kenichiro Aoki** received the B.S. and M.S. degrees in Mechanical Engineering from Keio University, Yokohama, Japan in 1998 and 2000, respectively. He joined Fujitsu Ltd., Kawasaki, Japan in 2000, where he has been engaged in research and development of numerical analysis technology for hard disk drives.

E-mail: aoki-k@jp.fujitsu.com